Measuring the Magnon-Photon Coupling in Shaped Ferromagnets: Tuning of the Resonance Frequency

Sergio Martínez-Losa del Rincón[1,2] Ignacio Gimeno,[1,2] Jorge Pérez-Bailón,[1,2]
Victor Rollano,[1,2] Fernando Luis,[1,2] David Zueco,[1,2] and María José Martínez-Pérez[1,2,*]

[1]*Instituto de Nanociencia y Materiales de Aragón (INMA), CSIC-Universidad de Zaragoza, Zaragoza, Spain*

[2]*Departamento de Física de la Materia Condensada, Universidad de Zaragoza, Zaragoza, Spain*

Cavity photons and ferromagnetic spin excitations can exchange information coherently in hybrid architectures, at speeds set by their mutual coupling strength. Speed enhancement is usually achieved by optimizing the geometry of the electromagnetic cavity. Here we show that the geometry of the ferromagnet also plays a role, by setting the fundamental frequency of the magnonic resonator. Using focused ion-beam patterning, we vary the aspect ratio of different Permalloy samples reaching operation frequencies above 10 GHz while working at low external magnetic fields. Additionally, we perform broadband ferromagnetic resonance measurements and cavity experiments that demonstrate that the light-matter coupling strength can be estimated using either open transmission lines or resonant cavities, yielding very good agreement. Finally, we describe a simple theoretical framework based on electromagnetic and micromagnetic simulations that successfully accounts for the experimental results. This approach can be used to design hybrid quantum systems exploiting magnetostatic mode excited in ferromagnets of arbitrary size and shape and to tune their operation conditions.

I. INTRODUCTION

In recent years, quantum manipulation and read-out protocols based on circuit quantum electrodynamics [1] have been successfully applied to the field of quantum magnonics [2–4]. In these studies, a coherent coupling between photons in an electromagnetic cavity and magnons in a ferromagnet is achieved in the strong [5,6], ultrastrong [7–9] and, even, close to the deep-strong regimes, [10]. This has opened the way to the observation of interesting phenomena with strong potential for applications like quantum transduction between optical and microwave photons [11,12], dispersive coupling between quantum systems [13–15], or nonreciprocal transmission of rf signals [16–19].

Electromagnetic cavities and ferromagnets are different versions of a harmonic oscillator, whose bosonic quanta of excitations correspond to photons and magnons, respectively. The resonant frequency of such cavities can be tuned by different means. This is relatively easy in the case of photons. For instance, size determines the fundamental modes in three-dimensional microwave cavities and superconducting coplanar waveguide (CPW) resonators [20]. Superconducting thin films are also used for the implementation of lumped-element LC resonators with fundamental

frequencies given by $\omega_p = 1/\sqrt{LC}$, which is, in essence, a geometrical factor as well [20]. In the case of soft magnets, spins precess around the local effective magnetic field. This field results from the contribution of the externally applied magnetic field B_{ext} and the (much more difficult to calculate) demagnetizing field [21]. Again, the latter is determined by the geometry of the sample. In isotropic magnets, e.g., spheres, shape effects cancel out and the resulting resonance frequency depends linearly on the external magnetic field as $\omega_m = \gamma_e B_{\text{ext}}$ [22] with $\gamma_e/2\pi = 28$ GHz/T the electron gyromagnetic ratio.

In most experiments performed so far, yttrium-iron-garnet (YIG) spheres strongly coupled to either three-dimensional cavities [5,9] or superconducting CPW resonators [13] have been the preferred choice. These magnets are commercial and exhibit record low Gilbert-damping constant ($\alpha \sim 10^{-5}$), which is beneficial for the observation of long-lived coherent exchange of information between the photonic and magnonic excitations. However, YIG spheres do not couple optimally to thin-film superconducting circuits that are pivotal in quantum applications [1,6]. YIG thin films are not easily compatible with conventional lithography processes [23] nor for cryogenic operation as the optimum substrate material for YIG growth becomes lossy with decreasing temperature [24]. For these reasons, other CMOS compatible materials like Permalloy (Py, with a moderate $\alpha \sim 10^{-2}$) [7,25–27] or

_____
*pemar@unizar.es

iron-cobalt alloys ($Fe_{75}Co_{25}$, with a very promising $\alpha \sim 10^{-3}$) are drawing attention [28,29].

Yet, custom tuning of the resonance frequency of such magnetic cavities is still to be demonstrated. This is relevant since experimental conditions usually impose certain constraints due to the use of, e.g., circulators or amplifiers with narrow frequency bandwidth. Additionally, operating devices at high frequencies is interesting since the coupling strength g between photons and magnons increases linearly with the frequency. The reason is that g is given by the Zeeman coupling between the magnon dipole moment and the oscillating vacuum field in the cavity. The latter is

$$b_{\text{rms}} = \sqrt{\frac{\mu_0 \hbar \omega_p}{2 V_{\text{eff}}}}, \quad (1)$$

where, the subindex denotes the rms and V_{eff} is the effective volume of the electromagnetic mode. V_{eff} depends on the size of the electromagnetic wavelength (thus on the inverse frequency) yielding $g \propto \omega_p$.

Increasing g is usually accomplished by a geometrical optimization of the resonator, i.e., patterning of nanoconstrictions [30–32] and/or reducing the impedance of lumped LC resonators, which is equivalent to reducing V_{eff} [8,33,34]. These approaches serve to confine b_{rms} within the (typically) small volume of the ferromagnet, yielding a square-root increase of the coupling. A larger (linear) enhancement of g should be achieved by working with high-frequency superconducting resonators. However, the experimental observation of such high-frequency effect in isotropic ferromagnets requires polarizing the magnetization with strong magnetic fields that are detrimental for the operation of superconducting circuits.

Here we show a direct way to tune the resonance frequency of suitably shaped micron-sized Py samples while keeping the external magnetic field below few tens of mT. Using superconducting CPW transmission lines we first show that, depending on the aspect ratio of the ferromagnet, the broadband ferromagnetic resonance (FMR) spectra can be modified at will. We then convert the transmission lines into cavities by opening gap capacitors. We demonstrate that both approaches can be used to experimentally estimate the coupling factors. Our experiments are complemented with a general-purpose theoretical model, including realistic electromagnetic and micromagnetic simulations that account for the nonhomogeneous spin precession along the volume of the ferromagnet.

II. RESULTS

A. Sample fabrication

We use four CPW superconducting transmission lines fabricated by optical lithography on 150-nm-thick niobium films deposited by sputtering onto single-crystal sapphire substrates [see Fig. 1(a) top]. A constriction of width w
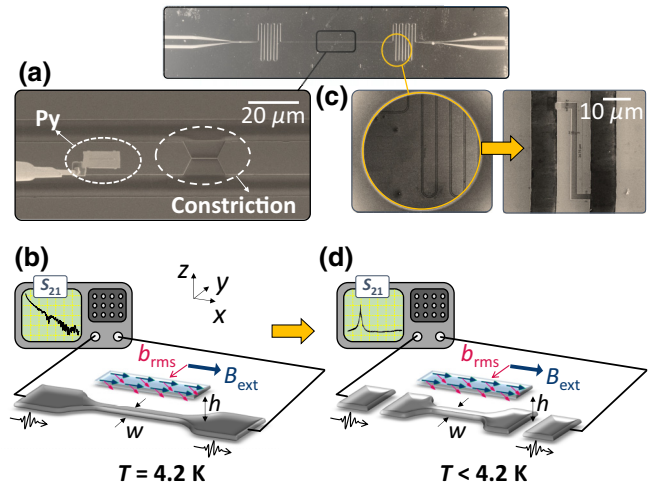

FIG. 1. (a) A constriction of width w is FIB patterned on the central part of a conventional Nb CPW transmission line. The Omniprobe needle is used to transport the Si_3N_4 palette with the Py ferromagnet towards the constriction. (b) Broadband FMR experiments are performed by measuring the S_{21} transmission parameter with a VNA while sweeping the external magnetic field B_{ext} applied along the $\hat{x}$ direction so that the microwave field b_{rms} produced by the transmission line is perpendicular to it. In this way, a quasihomogeneous Kittel magnon mode is excited in the ferromagnet (blue rectangle with colored arrows) lying at distance h from the superconductor. (c) Enlarged view of the meander region (left panel) where finger capacitors are opened by FIB (right panel). (d) The resulting CPW resonator, with characteristic frequency ω_p, and its coupling to the ferromagnetic sample are characterized using the VNA.

is opened in the central part of two transmission lines by focused ion-beam (FIB) milling using moderate currents, which result in lateral resolutions below 10 nm [see Fig. 1(a) bottom]. These constrictions, with dimensions matching those of the different samples, serve to locally focus b_{rms}, yielding enhanced coupling with the smallest ferromagnets.

On the other hand, Py thin films of various thicknesses t are e-beam evaporated onto 500-nm-thick Si_3N_4 membranes. The ferromagnets are patterned by FIB milling to produce four different samples labeled 1 to 4 whose dimensions are summarized in Fig. 2(a). Finally, an Omniprobe needle inside the FIB microscope is used to transport a micrometric sized Si_3N_4 palette containing the Py sample to precise positions on top of the superconducting circuit reaching optimum coupling [35]. For this purpose, it is useful to minimize the distance h between the ferromagnet and the superconducting line [Fig. 1(b)]. This is difficult in the case of sample 2 due to its large size that causes the Si_3N_4 palette to bend. We estimate $h \sim 4$ µm for sample 2 and $h \sim 500$ nm for the rest. Samples 1 and 2 are located onto the as-fabricated transmission lines, sample 3 goes onto
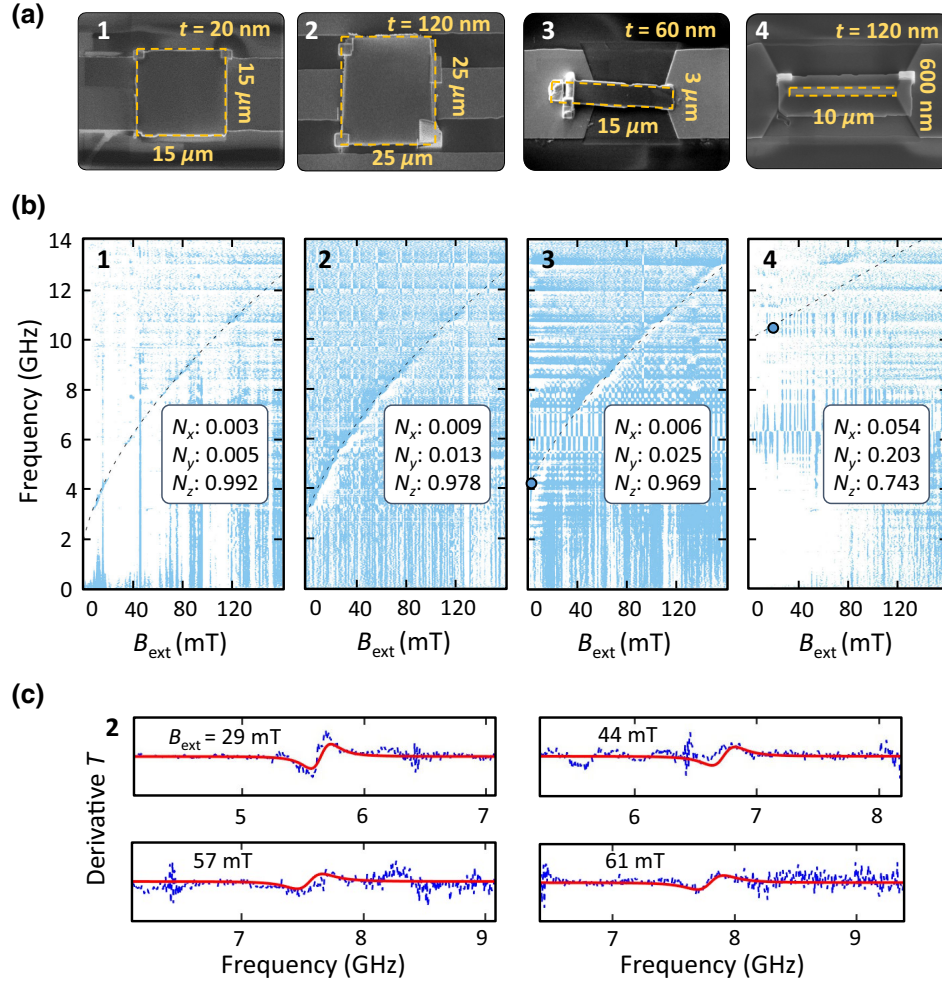
FIG. 2.   (a) SEM pictures of samples 1, 2, 3, and 4, highlighted with yellow dashed polygons, placed onto the central line of CPW superconducting transmission lines. (b) Broadband FMR curves of the same samples in derivative mode (see Sec. V). Fitting the magnon resonance frequency ω_m to the general Kittel formula [Eq. (2), dashed] yields the corresponding demagnetizing factors (legend). Color scale in all panels goes from -0.1 to 0.1. The solid dots in panels 3 and 4 correspond to the experimental data points obtained from cavity experiments [see Fig. 3(b)]. (c) Field derivative of the experimental transmission parameter (see Sec. V) corresponding to sample 2 (dashed blue) measured at different values of B_{ext} and fits based on Eq. (3) (solid red). Vertical scale goes from -1×10^{-3} to 1×10^{-3} in all panels.

the $w = 1$ μm wide constriction and, finally, sample 4 lies on top of the smallest $w = 240$ nm wide constriction [see Fig. 2(a)].

B. Broadband FMR

Samples are cooled down to 4.2 K in liquid helium in a cryostat containing a superconducting vector magnet. Broadband FMR experiments are performed by measuring the transmission coefficient S_{21} through the transmission line using a vector network analyzer (VNA) as schematized in Fig. 1(b). The external magnetic field B_{ext} is used to polarize the ferromagnet parallel to the transmission line ($\hat{x}$ direction) so that the microwave field produced by the superconductor (along the $\hat{y}$ direction) can excite the homogeneous Kittel mode with frequency given by [21]

$$\omega_m^2 = \gamma_e^2 \left[B_{ext} + (N_y - N_x)\mu_0 M_s \right]$$
$$\times \left[B_{ext} + (N_z - N_x)\mu_0 M_s \right] \quad (2)$$

Here, $\mu_0 = 4\pi \times 10^{-7}$ Tm/A and $M_s = 0.86 \times 10^6$ A/m is the saturation magnetization of Py measured in a nominally identical substrate. Finally, N_x, N_y, and N_z are the magnetometric demagnetizing factors that satisfy $N_x + N_y + N_z = 1$. These factors can be analytically estimated for each sample based on geometrical considerations [36]. Results are given in Table I.

Experimental curves corresponding to samples 1, 2, 3, and 4 are shown in Fig. 2(b). The Kittel resonance frequency depends strongly on the aspect ratio of the Py sample. As a matter of fact, ω_m increases from 2 GHz

TABLE I. Demagnetizing factors calculated from geometrical considerations [36] and fits based on Eq. (2).

	Calculated			Fitted		
	N_x	N_y	N_z	N_x	N_y	N_z
1	0.003	0.003	0.994	0.003	0.005	0.992
2	0.009	0.009	0.982	0.009	0.013	0.978
3	0.006	0.033	0.960	0.006	0.025	0.969
4	0.011	0.195	0.795	0.054	0.203	0.743

TABLE II. Photon resonance frequency (ω_p); photon-magnon coupling determined from FMR measurements (g_{FMR}), from cavity experiments (g_{res}) and from theory (g_{theo}). The latter is calculated for $h = 4\ \mu$m in the case of sample 2 and $h = 500$ nm for the rest.

	$\omega_p/2\pi$ (GHz)	$g_{FMR}/2\pi$ (MHz)	$g_{res}/2\pi$ (MHz)	$g_{theo}/2\pi$ (MHz)
1	2.8	7	...	6.6
2	3.5	16	...	17.3
3	4.2	36	36	45.0
4	10.5	66	72	72.4

up to more than 10 GHz at $B_{ext} \sim 0$ mT. Equation (2) accounts well for all experimental curves, allowing to fit the demagnetizing factors [see insets of Fig. 2(b) and Table I]. In the case of samples 1 and 2, symmetry considerations would yield $N_x = N_y$. However, this is not the case due to unavoidable imperfections that are especially dramatic in the case of sample 2 stemming from the above-mentioned bending. In the case of sample 3 and, especially, 4, N_y increases considerably, indicating that the $\hat{y}$ direction becomes progressively harder. As expected, N_x increases slightly with sample thickness. In the case of sample 4 we find N_x almost 5 times larger than the calculated value. This is probably due to a small misalignment of the external magnetic field with respect to the sample's easy axis. This effect is much more critical in samples with very large aspect ratio as 4.

FMR data allow us to estimate the frequency-dependent magnon-photon coupling. From input-output theory, we can express the transmission through an open line as [37]

$$T = 1 - \frac{\Gamma}{\Gamma + \gamma + i(\omega_m - \omega)}. \qquad (3)$$

We recall that ω_m depends on the magnetic field through Eq. (2). In the above formula, $\gamma = 2\alpha\omega_m$ is the linewidth of the ferromagnetic resonance and $\Gamma = g^2\pi/\omega_m$.

We use Eq. (3) to fit the experimental data (in derivative mode, as explained in Sec. V). A few representative curves corresponding to sample 2 are shown in Fig. 2(c). From these fits we estimate $\alpha \sim 0.01$, i.e., the Py damping factor at cryogenic temperatures. This value is close to the Gilbert-damping parameter measured at low and room temperatures [38]. On the other hand, we can estimate the frequency-dependent coupling g_{FMR} where the subindex is used to indicate that these values are obtained from FMR experiments. Table II gives coupling values determined at some fixed frequencies $\omega_m = \omega_p$.

C. Cavity experiments

We next transform each transmission line into a resonator by opening gap capacitors using FIB milling [see Fig. 1(c)]. In doing so, we choose the resulting cavity length to fit the $\lambda/2$ mode of the desired frequency ω_p summarized in Table II. Also, the capacitors are designed

to yield resonators with moderate quality factor $Q \sim 1 - 2 \times 10^3$, which are easier to measure while keeping $\kappa < \gamma$ [39]. Samples are again immersed in liquid helium except for sample 4 that is cooled down to 10 mK using a dilution refrigerator. A VNA is used to probe the S_{21} factor as a function of frequency while sweeping B_{ext} as described in the transmission line experiments [see Fig. 1(d)].

Measurements performed on 1 and 2 evidence that these samples are in the weak coupling regime. On the other hand, two avoided crossings can be distinguished in the experimental data obtained with samples 3 and 4 [see Fig. 3(a)]. These anticrossings appear at positive and negative magnetic fields, at the intersect with the FMR curves
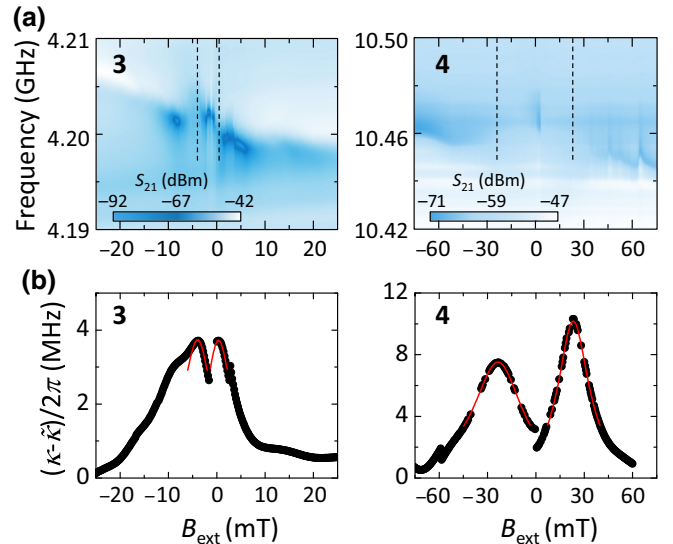

FIG. 3. (a) Experimental microwave transmission through superconducting resonators containing samples 3 ($\omega_p/2\pi = 4.2$ GHz, $T = 4.2$ K) and 4 ($\omega_p/2\pi = 10.5$ GHz, $T = 10$ mK). The dashed lines are the broadband FMR curves shown in Fig. 2(b). (b) Field dependence of the resonance width κ for the same resonators and least-squares fits (dashed lines) to Eq. (4). Data corresponding to sample 3 are shifted 2 mT towards negative fields due to a small remnant field in the superconducting coils. Maxima of κ versus B_{ext} provide two additional experimental points of FMR at $B_{ext} = -3.9$ and 0.4 mT for sample 3 and $B_{ext} = \pm 23$ mT for sample 4 [see Fig. 2(b)].

(dashed lines), which is a proof of magnon-photon coupling. In the case of sample 4, we observe also a number of small successive anticrossings at positive fields. The origin of such features is unknown but they might arise from the interaction between the fundamental mode of the resonator and spurious modes related with the magnetic behavior of the superconducting cavity itself, i.e., they are not related with the Permalloy sample.

Cavity experiments can be also used to give an alternative estimate of the magnon-photon coupling. For this purpose we analyze the cavity resonance linewidth κ as a function of external magnetic field. The linewidth is evaluated by fitting the experimental transmission to a Fano-like resonance (see Sec. V). The latter accounts better for asymmetries in our experimental data that likely arise from interference between the resonator and a small continuous background signal [40]. Depending on the coupling strength, the resonance broadens around the intersection field according to [41]

$$\kappa = \tilde{\kappa} + \frac{\gamma g^2}{(\omega_p - \omega_m)^2 + \gamma^2}, \qquad (4)$$

where $\tilde{\kappa}$ is the linewidth of the bare cavity that can be measured far from resonance. Again, we recall that ω_m depends on the external field through Eq. (2). Experimental κ versus B_{ext} curves exhibit two clear maxima at positive and negative fields, where level repulsion occurs [Fig. 3(b)]. Fitting these data to Eq. (4) gives a complementary estimate of the coupling (labeled g_{res}) that we summarize in Table II.

D. Theoretical model

We finish by comparing our experimental results with numerical estimations of the coupling factors. A generalization of formulas given in Refs. [42,43], where the field was considered homogeneous in the relevant region, follows. Each ferromagnetic sample is discretized into cells. The Hamiltonian interaction is given by $H_I = v_{\text{cell}} \sum_j \mathbf{m}_j \cdot \mathbf{b}_{\text{rms}}(\mathbf{r}_j)$. Here, v_{cell} and $\mathbf{m}_j$ are the volume and magnetization of the cell, respectively, while $\mathbf{b}_{\text{rms}}(\mathbf{r}_j)$ is the rms vacuum field at the cell's position $\mathbf{r}_j$. In each cell, the number of spins is large enough to perform the Holstein-Primakoff transformation, so the quantization of the magnetization can be written in terms of bosonic operators as $\mathbf{m}_j = \Delta\mathbf{M}_j(a_j^\dagger + a_j)$, where $\Delta\mathbf{M}_j$ is the position-dependent amplitude of the magnetization modulation. The latter will always be valid as we are working in the low photon or low power limit. Once this is done, we define the *collective* mode [44]:

$$a = \frac{1}{\sqrt{\sum_j \left(\Delta\mathbf{M}_j \cdot \mathbf{b}_{\text{rms}}(\mathbf{r}_j)\right)^2}} \sum_j \Delta\mathbf{M}_j \cdot \mathbf{b}_{\text{rms}}(\mathbf{r}_j) a_j.$$
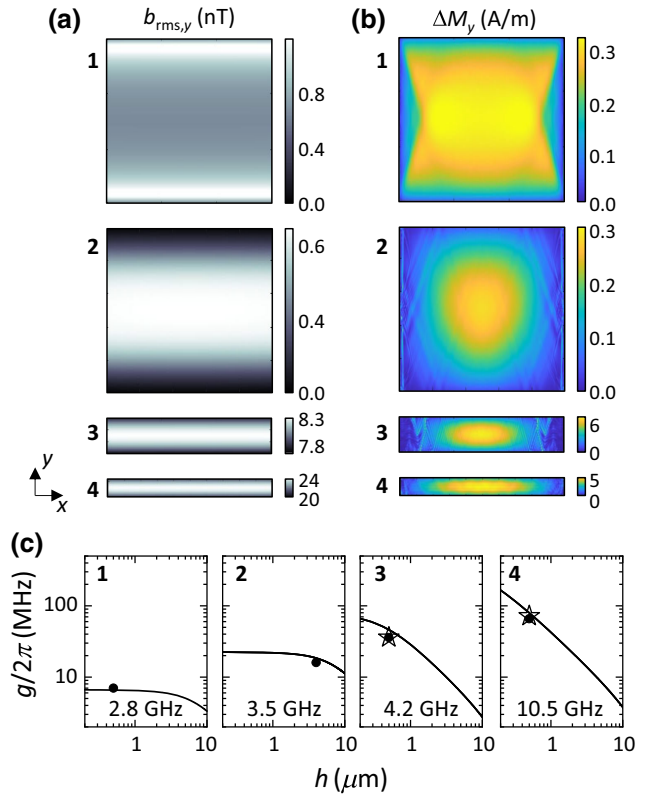

FIG. 4. Spatial distribution of the in-plane (y) component of b_{rms} (a) and ΔM (b) calculated at the position of the ferromagnet. (c) Solid lines are the numerical g_{theo} (at fixed frequency ω_p given above each panel) versus distance h. Data points are the experimental g_{FMR} (dots) and g_{res} (stars). From left to right, our experimental data roughly follow $g \propto \omega_p$.

Finally, taking the continuum limit, the magnon-resonator coupling reads

$$g^2 = \frac{\gamma v_{\text{cell}}}{4\hbar} \sum_j \mathbf{b}_{\text{rms}}(\mathbf{r}_j) \cdot \Delta\mathbf{M}_j, \qquad (5)$$

which is valid for *any* kind of magnonic mode excited in the ferromagnet, including the Kittel mode studied here.

We numerically calculate the spatial distribution of $\mathbf{b}_{\text{rms}}(\mathbf{r}_j)$ for the different resonators used in this work (see Sec. V). Figure 4(a) shows the resulting in-plane (y) component of b_{rms} for the different samples obtained at the position of the ferromagnet. We highlight that b_{rms} increases by a factor approximately 30 from sample 1 to 4 stemming from the smallness of the patterned constriction.

On the other hand, we need to estimate $\Delta\mathbf{M}_j$, which depends on the spatial distribution of the excitation field, i.e., $\mathbf{b}_{\text{rms}}(\mathbf{r}_j)$, and also on the nonhomogeneous magnetic susceptibility of the ferromagnet. Figure 4(b) shows the numerically calculated y component of ΔM for the different samples (see Sec. V). In general, ΔM_y is maximum

in the inner part of the ferromagnets but decreases considerably when approaching the edges. This effect is less pronounced in the case of sample 1, for which the susceptibility is substantially more homogeneous. This is due to its small thickness that constrains the modulation of the magnetization to the plane.

Finally, we use Eq. (5) to calculate the theoretical coupling factors g_{theo} at fixed frequency ω_p for varying distance between the ferromagnet and the superconducting line, i.e., distance h in Figs. 1(b) and 1(d). Results are plotted in Fig. 4(c) (solid lines) together with the experimental g values obtained at the same frequencies (scatter).

III. DISCUSSION

We start by highlighting that, in the case of samples 3 and 4, $g_{FMR} \approx g_{res}$. This demonstrates that the two experimental approaches, i.e., transmission and cavity configuration, are equivalent and valid to estimate the coupling. This result is not limited to the use of ferromagnetic samples but applies to any hybrid light-matter architecture based on, e.g., paramagnetic spins or superconducting qubits.

We can calculate the effective coupling per spin for samples 3 and 4 that amounts to 70 and 280 Hz, respectively. The latter approaches the largest spin-photon coupling strength achieved so far in optimized superconductor-peramalloy-insulator hybrid samples, i.e., 350 Hz [10] and exceeds the largest spin-photon coupling measured with paramagnetic spins under similar conditions [30]. As a matter of fact, the g values reported here are similar to those obtained using optimized LC resonators [25,33].

We next focus our attention on the experimental g_{FMR} and g_{res} and compare them to the g_{theo} calculated with our theory (Table II). The main source of error in g_{theo} is the distance h. As shown in Fig. 4(c), experiment and theory agree to a very good extent for the estimated values of h, confirming the validity of our model. Estimating the coupling strength in hybrid magnon-photon architectures is essential for designing reliable experiments. Here, we exploit the shape of thin-film ferromagnets as the tuning knob to modify their resonance frequency. This requires an additional account for the largely nonuniform demagnetizing field in rectangular prisms. However, little attention has been given till now to the distribution of magnetization precession along the volume of real ferromagnets [45,46]. In contrast, our approach involves the calculation of both the three-dimensional distribution of vacuum field created by the cavity and the magnetic susceptibility of the ferromagnet. This is worthwhile even for Kittel modes in ellipsoids of revolution but becomes critical when dealing with realistic thin films for which magnetization precession might be highly elliptical. Examples of the latter include spin modes in rectangular prisms but also skyrmions or flux-closure magnetic textures like vortices [42,43]. As we demonstrate, Eq. (5) can be used for calculating the coupling between superconducting circuits of whatever geometry and magnetostatic modes of any kind excited in ferromagnetic samples of arbitrary shape as long as this mode can be efficiently reproduced by micromagnetic simulations.

Finally, our experimental data serve to demonstrate the direct relation between the coupling strength and the cavity frequency [see Fig. 4(c)]. Deviations from the expected linear dependence arise from the different geometries of the resonators and the particular volumes and demagnetizing factors of each sample. The latter affects the magnetic susceptibility of the corresponding magnetostatic (Kittel) mode. Besides these factors, our experimental data roughly follow $g \propto \omega_p$. This is particularly evident for samples 3 and 4. Increasing the cavity operation frequency from $\omega_p/2\pi = 4.2$ GHz (sample 3) up to $\omega_p/2\pi = 10.5$ GHz (sample 4) yields twice the coupling strength.

We stress that patterning nanoconstrictions or reducing the impedance yields a square-root increase of g while keeping the losses in the ferromagnet unchanged, meaning these approaches serve to increase the cooperativity. On the other hand, increasing the operation frequency yields a linear increase of g, at the cost of also increasing $\gamma = 2\alpha\omega_p$. That is to say, increasing ω_p does not ease entering into the strong coupling regime but does have the effect of linearly increasing the rate of information exchange between photon and magnon excitations.

IV. CONCLUSIONS

We demonstrate the possibility of tuning the operation frequency in cavity magnonics by controlling the shape of the ferromagnet. Varying the aspect ratio of different Py samples we reach operation frequencies up to 10.5 GHz at approximately 20 mT. Working at such high frequencies with isotropic spherical ferromagnets would have required an external field close to 0.4 T. High-frequency operation together with the use of patterned nanoconstrictions in superconducting transmission lines enhances the net coupling between magnetic materials and cavity photons allowing us to reach an average single spin coupling of 280 Hz.

Our experimental results demonstrate that the light-matter coupling strength can be reliably estimated from both open transmission or cavity experiments. Besides, this has allowed combining broadband spectroscopic measurements, which provide the full picture of the ferromagnetic excitations, with experiments on superconducting resonators, which show how these modes couple to cavity photons.

Finally, we provide a simple recipe to theoretically calculate g in hybrid systems combining superconducting circuits and *realistic* ferromagnetic materials. Our approach can be used to design quantum magnonic experiments exploiting not only the homogeneous Kittel mode but

any higher-order magnonic mode in ferromagnets of arbitrary size and shape and to tune the operation conditions, frequency and magnetic field, to fit those required in a particular experiment or application.

V. METHODS

A. Data fitting

Open transmission data is analyzed by performing the pseudoderivative of the transmission parameter. For this purpose, we calculate

$$\text{Derivative } T_{\text{exp}} = \frac{T_{\text{exp}}(B_{\text{ext}}^{i+1}) - T_{\text{exp}}(B_{\text{ext}}^{i})}{T_{\text{exp}}(B_{\text{ext}}^{i+1})},$$

where T_{exp} is the linear amplitude of the transmission $T_{\text{exp}} = 10^{S_{21}/20}$ and superindexes i and $i+1$ refer to successive field values. Resulting curves versus frequency and field are plotted in Figs. 2(b) and 2(c). We then calculate the pseudoderivative of the absolute value of Eq. (3), which is given by

$$|T| = \sqrt{\frac{\gamma^2 + (\omega_m - \omega)^2}{\Gamma^2 + 2\Gamma\gamma + \gamma^2 + (\omega_m - \omega)^2}},$$

where ω_m and $\gamma = 2\alpha\omega_m$ are evaluated at each B_{ext}^i using Eq. (2). We finally fit the pseudoderivative of $|T|$ to the experimental data as shown in Fig. 2(c) to obtain the coupling strength $g = (\Gamma\omega_m/\pi)^{1/2}$.

Cavity experiments are analyzed by fitting the experimental resonance to a Fano curve:

$$T = y_0 + A\frac{\left[((\omega - \omega_0)/(\gamma/2)) + q\right]^2}{1 + \left((\omega - \omega_0)/(\gamma/2)\right)^2}\frac{1}{1 + q^2},$$

with y_0 an offset, A the amplitude, and q the Fano parameter that defines the lineshape of the resonance. Finally, $1/(1 + q^2)$ is a normalization factor. Fano resonances can be observed when the resonators are not perfectly matched to the input output lines, yielding a parasitic path between connectors. $q = 0$ yields an antiresonance whereas for $q \to \pm\infty$ the Lorentzian resonance with linewidth γ is recovered.

B. Simulations

The spatial distribution of $\mathbf{b}_{\text{rms}}(\mathbf{r}_j)$ is calculated using the finite-element software 3D-MLSI [47] that solves London equations in a user-defined superconducting circuit with flowing current i_{rms}. The latter is the rms zero-point

current that can be obtained as [48]

$$i_{\text{rms}} = \omega_p\sqrt{\frac{\hbar\pi}{4Z_0}}, \tag{6}$$

with $Z_0 = 50\ \Omega$ the impedance of the circuit. Inserting the experimental frequencies ω_p into Eq. (6), we calculate i_{rms} for each resonator. From here, 3D-MLSI allows calculating the spatial distribution of supercurrents and the resulting $\mathbf{b}_{\text{rms}}(\mathbf{r}_j)$ at each cell j inside the volume of the ferromagnet.

We finally calculate the spatial distribution of $\Delta\mathbf{M}_j$ resulting from the spatial-dependent $\mathbf{b}_{\text{rms}}(\mathbf{r}_j)$ using the micromagnetic solver MUMAX^3 [49]. For this purpose, we excite the ferromagnet with a time- and spatial-dependent field $\mathbf{b}_{\text{excit}} = \mathbf{b}_{\text{rms}}(\mathbf{r}_j)\cos(\omega_m t)$. As a result, we obtain the time evolution of the magnetization at each cell j and fit the resulting curve to an equation of the form $\Delta\mathbf{M}_j\sin(\omega_m t + \delta_j)$. The coupling is finally calculated applying Eq. (5).

[1] A. Blais, J. Gambetta, A. Wallraff, D. I. Schuster, S. M. Girvin, M. H. Devoret, and R. J. Schoelkopf, Quantum-information processing with circuit quantum electrodynamics, Phys. Rev. A **75**, 032329 (2007).

[2] M. Harder, B. M. Yao, Y. S. Gui, and C.-M. Hu, Coherent and dissipative cavity magnonics, J. Appl. Phys. **129**, 201101 (2021).

[3] Y. Li, W. Zhang, V. Tyberkevych, W.-K. Kwok, A. Hoffmann, and V. Novosad, Hybrid magnonics: Physics, circuits, and applications for coherent information processing, J. Appl. Phys. **128**, 130902 (2020).

[4] D. Lachance-Quirion, Y. Tabuchi, A. Gloppe, K. Usami, and Y. Nakamura, Hybrid quantum systems based on magnonics, Appl. Phys. Express **12**, 070101 (2019).

[5] Y. Tabuchi, S. Ishino, T. Ishikawa, R. Yamazaki, K. Usami, and Y. Nakamura, Hybridizing Ferromagnetic Magnons and Microwave Photons in the Quantum Limit, Phys. Rev. Lett. **113**, 083603 (2014).

[6] H. Huebl, C. W. Zollitsch, J. Lotze, F. Hocke, M. Greifenstein, A. Marx, R. Gross, and S. T. B. Goennenwein, High Cooperativity in Coupled Microwave Resonator Ferrimagnetic Insulator Hybrids, Phys. Rev. Lett. **111**, 127003 (2013).

[7] I. A. Golovchanskiy, N. N. Abramov, V. S. Stolyarov, M. Weides, V. V. Ryazanov, A. A. Golubov, A. V. Ustinov, and M. Y. Kupriyanov, Ultrastrong photon-to-magnon coupling in multilayered heterostructures involving superconducting coherence via ferromagnetic layers, Sci. Adv. **7**, eabe8638 (2021).

[8] G. Flower, M. Goryachev, J. Bourhill, and M. E. Tobar, Experimental implementations of cavity-magnon systems from ultra strong coupling to applications in precision measurement, New J. Phys. **21**, 095004 (2019).

[9] X. Zhang, C.-L. Zou, L. Jiang, and H. X. Tang, Strongly Coupled Magnons and Cavity Microwave Photons, Phys. Rev. Lett. **113**, 156401 (2014).

[10] I. Golovchanskiy, N. Abramov, V. Stolyarov, A. Golubov, M. Y. Kupriyanov, V. Ryazanov, and A. Ustinov, Approaching Deep-Strong On-Chip Photon-to-Magnon Coupling, Phys. Rev. Appl. **16**, 034029 (2021).

[11] N. J. Lambert, A. Rueda, F. Sedlmeir, and H. G. L. Schwefel, Coherent conversion between microwave and optical photons—An overview of physical implementations, Adv. Quantum Technol. **3**, 1900077 (2020).

[12] R. Hisatomi, A. Osada, Y. Tabuchi, T. Ishikawa, A. Noguchi, R. Yamazaki, K. Usami, and Y. Nakamura, Bidirectional conversion between microwave and light via ferromagnetic magnons, Phys. Rev. B **93**, 174427 (2016).

[13] Y. Li, V. G. Yefremenko, M. Lisovenko, C. Trevillian, T. Polakovic, T. W. Cecil, P. S. Barry, J. Pearson, R. Divan, V. Tyberkevych, C. L. Chang, U. Welp, W.-K. Kwok, and V. Novosad, Coherent Coupling of Two Remote Magnonic Resonators Mediated by Superconducting Circuits, Phys. Rev. Lett. **128**, 047701 (2022).

[14] D. Lachance-Quirion, S. P. Wolski, Y. Tabuchi, S. Kono, K. Usami, and Y. Nakamura, Entanglement-based single-shot detection of a single magnon with a superconducting qubit, Science **367**, 425 (2020).

[15] S. Wolski, D. Lachance-Quirion, Y. Tabuchi, S. Kono, A. Noguchi, K. Usami, and Y. Nakamura, Dissipation-Based Quantum Sensing of Magnons with a Superconducting Qubit, Phys. Rev. Lett. **125**, 117701 (2020).

[16] Y.-Y. Wang, S. van Geldern, T. Connolly, Y.-X. Wang, A. Shilcusky, A. McDonald, A. A. Clerk, and C. Wang, Low-Loss Ferrite Circulator as a Tunable Chiral Quantum System, Phys. Rev. Appl. **16**, 064066 (2021).

[17] N. Zhu, X. Han, C.-L. Zou, M. Xu, and H. X. Tang, Magnon-photon strong coupling for tunable microwave circulators, Phys. Rev. A **101**, 043842 (2020).

[18] X. Zhang, A. Galda, X. Han, D. Jin, and V. M. Vinokur, Broadband Nonreciprocity Enabled by Strong Coupling of Magnons and Microwave Photons, Phys. Rev. Appl. **13**, 044039 (2020).

[19] Y.-P. Wang, J. Rao, Y. Yang, P.-C. Xu, Y. Gui, B. Yao, J. You, and C.-M. Hu, Nonreciprocity and Unidirectional Invisibility in Cavity Magnonics, Phys. Rev. Lett. **123**, 127202 (2019).

[20] D. M. Pozar, *Microwave Engineering*, 4th ed. (Wiley, USA, 2011).

[21] C. Kittel and D. F. Holcomb, Introduction to solid state physics, Am. J. Phys. **35**, 547 (1967).

[22] L. R. Walker, Magnetostatic modes in ferromagnetic resonance, Phys. Rev. **105**, 390 (1957).

[23] P. G. Baity, D. A. Bozhko, R. Macêdo, W. Smith, R. C. Holland, S. Danilin, V. Seferai, J. Barbosa, R. R. Peroor, S. Goldman, U. Nasti, J. Paul, R. H. Hadfield, S. McVitie, and M. Weides, Strong magnon–photon coupling with chip-integrated YIG in the zero-temperature limit, Appl. Phys. Lett. **119**, 033502 (2021).

[24] L. Mihalceanu, V. I. Vasyuchka, D. A. Bozhko, T. Langner, A. Y. Nechiporuk, V. F. Romanyuk, B. Hillebrands, and A. A. Serga, Temperature-dependent relaxation of dipole-exchange magnons in yttrium iron garnet films, Phys. Rev. B **97**, 214405 (2018).

[25] J. T. Hou and L. Liu, Strong Coupling Between Microwave Photons and Nanomagnet Magnons, Phys. Rev. Lett. **123**, 107702 (2019).

[26] Y. Li, T. Polakovic, Y.-L. Wang, J. Xu, S. Lendinez, Z. Zhang, J. Ding, T. Khaire, H. Saglam, R. Divan, J. Pearson, W.-K. Kwok, Z. Xiao, V. Novosad, A. Hoffmann, and W. Zhang, Strong Coupling Between Magnons and Microwave Photons in On-Chip Ferromagnet-Superconductor Thin-Film Devices, Phys. Rev. Lett. **123**, 107701 (2019).

[27] I. A. Golovchanskiy, N. N. Abramov, V. S. Stolyarov, I. V. Shchetinin, P. S. Dzhumaev, A. S. Averkin, S. N. Kozlov, A. A. Golubov, V. V. Ryazanov, and A. V. Ustinov, Probing dynamics of micro-magnets with multi-mode superconducting resonator, J. Appl. Phys. **123**, 173904 (2018).

[28] I. Haygood, M. Pufall, E. Edwards, J. M. Shaw, and W. Rippard, Strong Coupling of an Fe-Co Alloy with Ultralow Damping to Superconducting Co-Planar Waveguide Resonators, Phys. Rev. Appl. **15**, 054021 (2021).

[29] M. A. W. Schoen, D. Thonig, M. L. Schneider, T. J. Silva, H. T. Nembach, O. Eriksson, O. Karis, and J. M. Shaw, Ultra-low magnetic damping of a metallic ferromagnet, Nat. Phys. **12**, 839 (2016).

[30] I. Gimeno, W. Kersten, M. C. Pallarés, P. Hermosilla, M. J. Martínez-Pérez, M. D. Jenkins, A. Angerer, C. Sánchez-Azqueta, D. Zueco, J. Majer, A. Lostao, and F. Luis, Enhanced molecular spin-photon coupling at superconducting nanoconstrictions, ACS Nano **14**, 8707 (2020).

[31] P. Haikka, Y. Kubo, A. Bienfait, P. Bertet, and K. Mølmer, Proposal for detecting a single electron spin in a microwave resonator, Phys. Rev. A **95**, 022306 (2017).

[32] M. D. Jenkins, U. Naether, M. Ciria, J. Sesé, J. Atkinson, C. Sánchez-Azqueta, E. del Barco, J. Majer, D. Zueco, and F. Luis, Nanoscale constrictions in superconducting coplanar waveguide resonators, Appl. Phys. Lett. **105**, 162601 (2014).

[33] S. Probst, A. Bienfait, P. Campagne-Ibarcq, J. J. Pla, B. Albanese, J. F. D. S. Barbosa, T. Schenkel, D. Vion, D.

Esteve, K. Mølmer, J. J. L. Morton, R. Heeres, and P. Bertet, Inductive-detection electron-spin resonance spectroscopy with 65 spins/Hz sensitivity, Appl. Phys. Lett. **111**, 202604 (2017).

[34] C. Eichler, A. Sigillito, S. Lyon, and J. Petta, Electron Spin Resonance at the Level of 10^4 Spins using Low Impedance Superconducting Resonators, Phys. Rev. Lett. **118**, 037701 (2017).

[35] M. J. Martínez-Pérez, J. Pablo-Navarro, B. Müller, R. Kleiner, C. Magén, D. Koelle, J. M. de Teresa, and J. Sesé, NanoSQUID magnetometry on individual as-grown and annealed co nanowires at variable temperature, Nano Lett. **18**, 7674 (2018).

[36] A. Aharoni, Demagnetizing factors for rectangular ferro-magnetic prisms, J. Appl. Phys. **83**, 3432 (1998).

[37] D. Roy, C. Wilson, and O. Firstenberg, Colloquium: Strongly interacting photons in one-dimensional contin-uum, Rev. Mod. Phys. **89**, 021001 (2017).

[38] Y. Zhao, Q. Song, S.-H. Yang, T. Su, W. Yuan, S. S. P. Parkin, J. Shi, and W. Han, Experimental investigation of temperature-dependent Gilbert damping in permalloy thin films, Sci. Rep. **6**, 22890 (2016).

[39] M. Göppl, A. Fragner, M. Baur, R. Bianchetti, S. Filipp, J. M. Fink, P. J. Leek, G. Puebla, L. Steffen, and A. Wall-raff, Coplanar waveguide resonators for circuit quantum electrodynamics, J. Appl. Phys. **104**, 113904 (2008).

[40] U. Fano, Effects of configuration interaction on intensities and phase shifts, Phys. Rev. **124**, 1866 (1961).

[41] P. Bushev, A. K. Feofanov, H. Rotzinger, I. Protopopov, J. H. Cole, C. M. Wilson, G. Fischer, A. Lukashenko, and A. V. Ustinov, Ultralow-power spectroscopy of a rare-earth spin ensemble using a superconducting resonator, Phys. Rev. B **84**, 060501 (2011).

[42] M. J. Martínez-Pérez and D. Zueco, Quantum electrody-namics with magnetic textures, New J. Phys. **21**, 115002 (2019).

[43] M. J. Martínez-Pérez and D. Zueco, Strong coupling of a single photon to a magnetic vortex, ACS Photonics **6**, 360 (2018).

[44] T. Hümmer, G. M. Reuther, P. Hänggi, and D. Zueco, Nonequilibrium phases in hybrid arrays with flux qubits and nitrogen-vacancy centers, Phys. Rev. A **85**, 052320 (2012).

[45] R. Macêdo, R. C. Holland, P. G. Baity, L. J. McLellan, K. L. Livesey, R. L. Stamps, M. P. Weides, and D. A. Bozhko, Electromagnetic Approach to Cavity Spintronics, Phys. Rev. Appl. **15**, 024065 (2021).

[46] J. Bourhill, V. Castel, A. Manchec, and G. Cochet, Univer-sal characterization of cavity–magnon polariton coupling strength verified in modifiable microwave cavity, J. Appl. Phys. **128**, 073904 (2020).

[47] M. M. Khapaev, M. Y. Kupriyanov, E. Goldobin, and M. Siegel, Current distribution simulation for superconducting multi-layered structures, Supercond. Sci. Technol. **16**, 24 (2002).

[48] M. Jenkins, T. Hümmer, M. J. Martínez-Pérez, J. García-Ripoll, D. Zueco, and F. Luis, Coupling single-molecule magnets to quantum circuits, New J. Phys. **15**, 095007 (2013).

[49] A. Vansteenkiste, J. Leliaert, M. Dvornik, M. Helsen, F. Garcia-Sanchez, and B. V. Waeyenberge, The design and verification of MuMax3, AIP Adv. **4**, 107133 (2014).